Received: 9 February 2023 | Revised: 18 May 2023 | Accepted: 23 May 2023

CAAI Transactions on Intelligence Technology

DOI: 10.1049/cit2.12254

ORIGINAL RESEARCH

An efficient deep learning model for brain tumour detection with privacy preservation

Mujeeb Ur Rehman[1] | Arslan Shafique[1] | Imdad Ullah Khan[2] | Yazeed Yasin Ghadi[3] | Jawad Ahmad[4] | Mohammed S. Alshehri[5] | Mimonah Al Qathrady[6] | Majed Alhaisoni[7] | Muhammad H. Zayyan[8]

[1]School of Science, Technology and Health, York St John University, York, UK

[2]Department of Computer Science, Lahore University of Management Sciences, Lahore, Pakistan

[3]Department of Computer Science, Al Ain University, Abu Dhabi, United Arab Emirates

[4]School of Computing, Engineering and the Built Environment, Edinburgh Napier University, Edinburgh, UK

[5]Department of Computer Science, College of Computer Science and Information Systems, Najran University, Najran, Saudi Arabia

[6]Department of Information Systems, College of Computer Science and Information Systems, Najran University, Najran, Saudi Arabia

[7]Computer Sciences Department, College of Computer and Information Sciences, Princess Nourah Bint Abdulrahman University, Riyadh, Saudi Arabia

[8]Computer Science Department, Faculty of Computers and Information Sciences, Mansoura University, Mansoura, Egypt

Correspondence
Jawad Ahmad.
Email: J.Ahmad@napier.ac.uk

Funding information
Najran University

Abstract

Internet of medical things (IoMT) is becoming more prevalent in healthcare applications as a result of current AI advancements, helping to improve our quality of life and ensure a sustainable health system. IoMT systems with cutting-edge scientific capabilities are capable of detecting, transmitting, learning and reasoning. As a result, these systems proved tremendously useful in a range of healthcare applications, including brain tumour detection. A deep learning-based approach for identifying MRI images of brain tumour patients and normal patients is suggested. The morphological-based segmentation method is applied in this approach to separate tumour areas in MRI images. Convolutional neural networks, such as LeNET, MobileNetV2, Densenet and ResNet, are tested to be the most efficient ones in terms of detection performance. The suggested approach is applied to a dataset gathered from several hospitals. The effectiveness of the proposed approach is assessed using a variety of metrics, including accuracy, specificity, sensitivity, recall and F-score. According to the performance evaluation, the accuracy of LeNET, MobileNetV2, Densenet, ResNet and EfficientNet is 98.7%, 93.6%, 92.8%, 91.6% and 91.9%, respectively. When compared to the existing approaches, LeNET has the best performance, with an average of 98.7% accuracy.

KEYWORDS
data privacy, deep learning, machine learning, medical image processing

1 | INTRODUCTION

There is an increasing global trend of using information and communication technology in providing healthcare services [1–6]. Machine learning and data science in general and image processing, in particular, are playing a vital role in non-invasive medical diagnostics for various diseases [7]. These tools are employed to diagnose tumours in the brain, lung, and liver [8].

A brain tumour is an abnormal growth inside the brain tissues. It can spread tumour tissue to other cells in the same area [9]. Based on their location and size in relation to form functions in the brain area, the cells in this portion of the brain are commonly categorised into grey matter (g), white matter (w) and cerebrospinal fluid (CSF) [10–12]. Improper blood flow in the blood arteries and hereditary disorders may have an effect on these cells in the brain, which may cause brain tumours. According to data from the World Health Organization and National Cancer Institute (NCI), 12765 people are infected by brain tumours every year globally [13]. Early identification of cancerous spots can greatly help contain the spread of cancerous areas to neighbouring cells.

Various invasive and non-invasive methods are used to detect a tumour in brain imaging [14–16]. In invasive procedures, an extraneous material is introduced into the human brain to detect and localise any abnormal growth in the brain regions. These procedures require more time to discover the tumour cells and result in a significant degree of discomfort blood loss. Non-invasive methods identify and localise brain tumours in scans such as Magnetic Resonance Imaging (MRI) and Computer Tomography (CT). CT identifies only soft tissues, as seen in Figure 1a and is incompatible with hard tissues such as the human skull [17]. MRI scans, on the other hand, detect both hard and soft tissues and is more appropriate for scanning the interior parts of the human brain, as seen in Figure 1b.

Brain MRI images (BMIs) are classified into three types depending on the contrast evaluation in image areas: diffusion inverted recovery, T1 and T2 weighted types and diffusion-weighted types [18]. The tumour's images are classified into two groups based on the severity of the tumours: main tumours and secondary tumours. Figure 2 depicts an MRI scan of the brain damaged by the tumour. We identify the following key tasks and challenges for an automatic physician's decision support system to identify and localise brain tumours in BMIs.

Task 1: Data Availability It is well-known in the machine learning community that deep learning is a very data-hungry approach. For high accuracy and reliability, the classifier needs to be trained by a diverse and extensive set of labelled BMIs. These BMIs need to be labelled by specialist doctors; hence, a large comprehensive dataset is very costly. In the proposed work a primary dataset in the form of digital images is used containing 255 BMIs. We have supplemented the primary dataset with 4169 more images collected from various hospitals. However, the total number of BMIs (4424) is still insufficient to feed it into the deep learning framework. The challenge is an intelligent data augmentation scheme that inflates the dataset with more reliable samples.

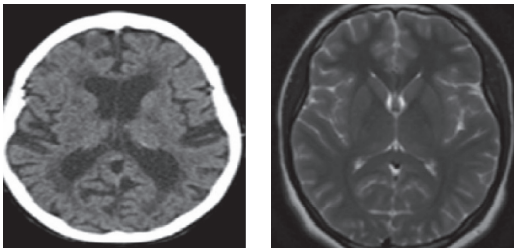

(a) CT image (b) MRI image

FIGURE 1 Brain scans.

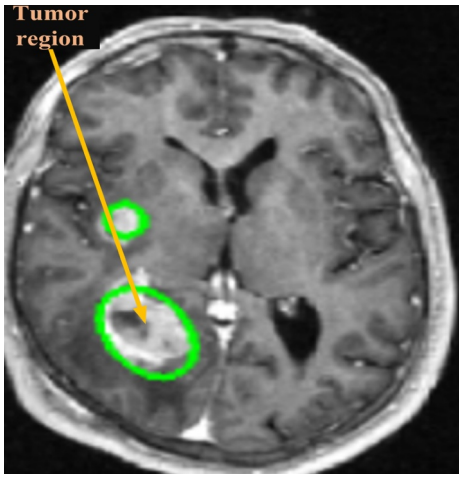

FIGURE 2 Tumour spotted in a BMI.

Task 2: Patients Privacy and Data Security According to the American Medical Association, medical images used in the dataset may include sensitive and secret information [19, 20]. Unauthorised access to a computer system may result in the theft of private data or the misuse of intimate images. Using illegal images or altered data may result in significant legal and medical consequences. Therefore, any BMI classification system must include a data security and privacy-preserving mechanism. Due to the unique features of image data that distinguish it from text structure data such as high redundancy and correlation and large storage capacity, traditional encryption schemes such as Data Encryption Standard (DES) [21] and Advanced Encryption Standard (AES) [22] have been used in recent years to protect sensitive images from eavesdroppers. The large number of encryption rounds in such algorithms renders the resulting system computationally infeasible. It is critical to secure such medical images using a lightweight encryption technique based on chaotic maps, such as the hyper-chaotic map.

Task 3: Classification In recent years, traditional classification algorithms such as K-nearest neighbour (*k*NN), random forest (RF), support vector machine (SVM), and neural networks (NN) have been used to detect brain tumours in BMIs [23]. Such algorithms have poor training and testing speeds and require a large number of BMIs with distinct enhancement patterns. Due to over-fitting issues during the training and testing phases of traditional classifiers, their complexity is significant [24].

This paper proposes novel techniques to tackle all these three challenges. We devise a convolutional neural network-based deep learning architecture for BMI classification. For BMIs with tumours, we apply morphological segmentation to localize the tumour and identify the infected region. Our system removes noise from BMIs, then employs a CNN-based classifier to produce low-contrast brain images and improves the accuracy of tumour classification and segmentation. We also design a lightweight encryption scheme based on chaotic maps that is computationally efficient. We perform extensive empirical evaluation and thoroughly compare it with various deep learning and non-deep learning-based classifiers. We designed a data augmentation strategy incorporating interpolation and data flipping that add more labelled and reliable images to the primary dataset for the improved the classification performance. We provide a schematic summary of the proposed work in Figure 3.

The main features of this work are:

For data availability challenges

- We collected a large number of BMI scans from various hospitals and got them labelled by specialist doctors.
- To further boost the accuracy of deep learning models, we propose a data augmentation scheme, which adds more training images using data interpolation and data flipping techniques.

For data security challenges

- We compare chaotic logistic and hyperchaotic maps to analyse their security and computational complexity.
- We develop a novel and computationally efficient cryptographic scheme to protect BMIs from eavesdroppers.
- We evaluate the security of our scheme using multiple parameters, such as entropy, contrast, mean square error and peak signal-to-noise ratio. We demonstrate the effectiveness of the proposed work compared to existing encryption schemes.

For classification challenges

- We implemented several CNN architectures, such as MobileNetV2, Densenet, ResNet, LeNET and EfficientNet to identify tumours in the BMIs. We demonstrate that LeNET significantly outperforms other architectures in terms of classification.
- We devised a method for accurately predicting the occurrence of tumour regions in BMIs. The proposed technology may be deployed using a smartphone application.

The rest of the paper is organised as follows: Section 2 provides an overview of existing work. In Section 3, we provide the details of the dataset. Section 4 and Section 5 are devoted to the details of the proposed encryption scheme and classification methodology, respectively. Section 6 explains the measure used to evaluate our proposed technique. Section 7 provide the results of the empirical evaluation of our method and its comparison with the existing methods. We conclude the paper in Section 8.

2 | RELATED WORK

This section provides an overview of the existing work related to data security and classification tasks. In the last several decades, chaos theory has been extensively utilised in the field of data security [25–30]. Due to the tremendous chaos properties, such as key sensitivity, difficulty to predict and large keyspace, it has been used to secure the sensitive images in the domains of military and medical sciences. Girdhar et al. [31] proposed an image encryption approach employing three unique chaotic maps to increase the security of the image. One of their key objectives is to minimise processing time. They also included confusion and permutation operations, performed independently, which results in a slight increase in processing time. While the proposed encryption algorithm's degree of security is adequate, it is unsuitable for real-time applications such as drone applications that demand rapid reaction. This

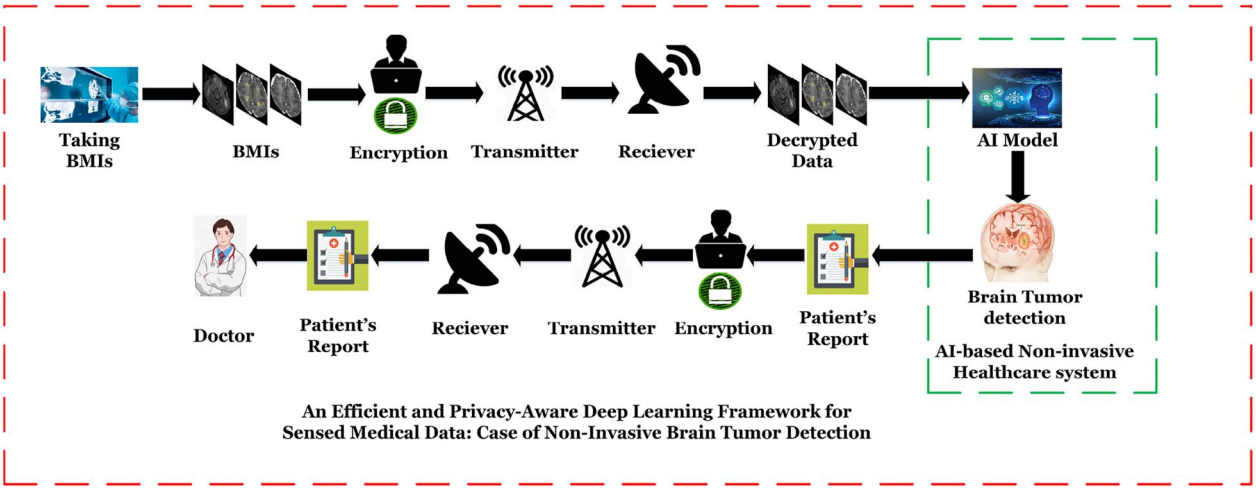

FIGURE 3 Proposed architecture.

vulnerability may be avoided by running all operations in their algorithms in parallel.

Talhaoui et al. [32] proposed a novel one-dimensional fractional chaotic map with a vast chaotic range. The suggested map has a higher degree of chaos than traditional maps such as the chaotic logistic and chaotic sine maps. The authors used their chaotic map for image encryption achieving a suitable level of security. In Ref. [33], Ravichandran et al. used shuffling and diffusion in their encryption scheme. They incorporate two primary phases of confusion and diffusion and the integration of chaotic maps. These phases are run sequentially, which increases the encryption algorithm's computing time. To further strengthen the security of the encryption scheme, Bhogal et al. [34] proposed to encrypt the digital images using a chaotic map which also incorporates AES. The comparison results demonstrate that their approach performs better than AES, but the many encryption rounds included in their scheme require a significant amount of computational time to complete encryption.

Many machine learning algorithms and image processing techniques have been utilised to detect brain tumours in BMIs. Bansal et al. [35] applied a segmentation process in which a classification algorithm based on the swarm ant lion is incorporated. As a part of this strategy, canny edge detection is used on primary BMIs to segment tumour areas. The swarm optimisation technique was used with this non-linear approach to obtain statistically meaningful simulation results. On the BMIs from the BRATS 2015 dataset, an open-access dataset, the authors achieved 98.5% accuracy in tumour segmentation. Rajagopal [36] devised a technique for detecting brain tumours using machine learning methods. This approach used an energy segmentation algorithm on a series of BMIs to find tumour patterns in them. Using a random forest (RF) classifier, the segmented tumour regions are divided into normal and aberrant tumour regions. Deep learning-based techniques have been used for image classification with promising results. However, a drawback of medical image categorisation is the limited size of the medical images dataset. To overcome this problem, Deepka et al. [37] used a combination of CNN features and support vector machine (SVM) categorisation to automate the classification of medical images. Their model achieved a classification accuracy of 95.82%. Lorenzo et al. [38] proposed a novel deep learning strategy for segmenting brain tumours using fluid reduction inversion recovery using MRI and CNN. Due to the scarcity of accessible data, they trained their suggested models using only positive cases. The proposed model was time-efficient but failed to correctly classify the tumour cases from non-tumour cases.

Hashihezi et al. [39] utilised MRI images to train a novel hybrid model that combines CNN with neural autoregressive distribution estimation (NADE). They evaluate the model on 3064 contrast-enhanced BMIs of three different kinds of brain tumours. The accuracy of correctly classifying images with tumours was 91.5%, which is below the acceptable level of accuracy. Khan et al. [40] classified BMIs into tumour and non-tumour using a CNN-based technique combined with data augmentation and image processing. The performance of proposed model was compared to pre-trained ResNet-50, VGG-16 and Inception-v3 models using transfer learning. On a relatively short dataset, the accuracy of ResNet-50, VGG-16 and Inception-V3 was 89%, 96% and 75%, respectively. Bousselham et al. [41] examined the performance of an approach used for the generation of thermal maps, which is ultimately used to identify tumour patterning cells in the human cerebral cortex. The anomalous zones with inner borders are discovered using the thermal map. A technique developed by Ailqazzaz et al. [13] used a logistic regression approach by altering their linear characteristics to detect pixels in BMIs with tumour patterns. They confirmed the simulation findings of their approach using a k-fold testing methodology. Alqudah et al. [42] developed a deep learning architecture for the classification and detection of brain tumours. Deep learning has also been successfully utilised to classify gliomas, meningiomas and pituitary tumours. It has been established that analysing the uncropped and cropped areas in the categorised brain images increased the accuracy of tumour region segmentation by around 20%.

Sheela et al. [43] incorporated a morphological edge detection approach to identify and segment regions in the BMIs where tumour-affected pixels lie. The fuzzy C-mean technique is employed to discover areas in BMIs with aberrant pixels; subsequently, morphological processes are used to separate tumour pixels from their neighbouring normal pixels by using regions in the image that contain aberrant pixels. Rao et al. [44] employed the conditional random field (CRF) classification algorithm. They extracted features relevant to the energy functions from BMIs and used these functions to segment the aberrant pixels from the rest of the image. The CRF technique is used to classify these energy functions of the training samples. Furthermore, morphological processes such as dilation and erosion are used to segment cancer pixels, resulting in the segmentation of tumour pixels.

Asikala et al. [45] extracted the non-linear wavelet features by applying a statistical transformation to brain modality. The non-linear features of the various kinds of brain cells are reflected in the wavelet features calculated for each type of brain cell. The wavelet coefficients from BMIs are classified using an artificial neural network framework. Morphological techniques are also applied to segment tumour pixels. Using this wavelet approach, the authors achieved an average classification accuracy of 98%.

The modified version of the Alex Krizhevsky network (AlexNet) [46] is trained on BMIs by Khawaldeh et al. [47] to construct the CNN architecture. Their CNN architecture achieved 91.6% of the average segmentation accuracy. Using CNN architecture, Pereira et al. [48] identified abnormal or tumour tissue patterns in BMIs. Their framework achieved an 89.5% abnormality area identification rate - the best for high-resolution situations. Using a discriminative clustering technique, Kong et al. [49] successfully identified tumour cells in a large collection of BMIs. This technique first generates random characteristics from the BMIs, after which discriminative methods are employed on the segmented and clustered areas of the brain MRI images. Their approach successfully recognises 95% BMIs. A

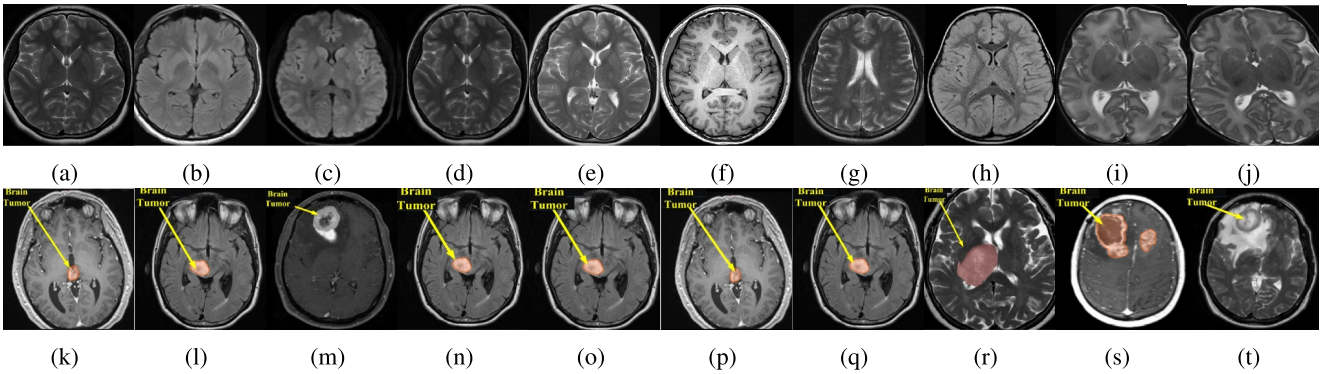

FIGURE 4 BMIs of normal person (a)–(j) and patient with brain tumour (k)–(t) collected from various hospitals.

BMI is used by Islam et al. [50] to collect multi-fractal texture data, which is then used to find the non-linearity of the pixels in the BMI. The generated features are then categorised using a real-time classification magnitude technique.

3 | DATA AUGMENTATION

Deep learning is inherently data-hungry; it is well-known that the larger number of training instances yields higher accuracy in deep learning models. An extensive and diverse set of labelled BMIs is required to achieve reliable results. The collection of comprehensive and large datasets is very costly because the labelling of BMIs is done by specialist doctors [51]. A sample of collected images related to normal patients and patients with brain tumours is shown in Figure 4.

To achieve the maximum possible classification accuracy from our architecture, we augment our dataset with additional training BMIs. We employ two widely-used methods to augment the training data: (a) data interpolation and (b) data flipping at different orientations. We augment the data before any pre-processing and data preparation for analysis. This is so because both data interpolation and data flipping add noise to the synthetic images. We deal with noise in the preprocessing phase.

3.1 | Data interpolation

In data interpolation, an average of any two real instances is computed, and the new (synthetic) instance is added to the dataset [52].

3.2 | Data flipping

After the interpolation phase, a few images from the datasets are flipped to various orientations (25, 45, 60 and 75). The original images and flipped versions are shown in Figure 5. These flipped versions of the original images are put near the end of the dataset, which is also the portion of the dataset that is utilised in this proposed study. Despite the fact that none of the data inflation approaches provided the original data, the new data points that are produced using such techniques are highly similar to the original data points. The data interpolation and flipping techniques are summarised in the pseudo-code given in Algorithm 1.

Algorithm 1 Pseudo code for interpolation and data flipping

Start
$L \leftarrow$ dataset length
Data inflation:
for $i = 1 \rightarrow L$ **do**
    $New_i = \frac{M_{im}(i)+M_{im}(i+1)}{2}$ ▷ Generate new images
Data flipping:
for $i = 1 \rightarrow L/4$ **do**
    $Newf1_i \leftarrow \frac{M_{im}}{i}$
for $i = L/4 \rightarrow L/2$ **do**
    $Newf1_i \leftarrow \frac{M_{im}}{i}$
for $i = L/2 \rightarrow 3\ L/4$ **do**
    $Newf1_i \leftarrow \frac{M_{im}}{i}$
for $i = 3\ L/4 \rightarrow L$ **do**
    $Newf1_i \leftarrow \frac{M_{im}}{i}$
Output: Data Augmented BMIs.
End

4 | ENCRYPTION SCHEME

Medical images have become the most extensively utilised information in healthcare informatics. In many cases, images are stored and processed on a remote cloud server. Such images are inevitably threatened by security flaws entailing various forms of harm ranging from individual privacy violations to life-threatening data alteration [53–56]. As a result, the security of digital images has become a challenging task for researchers. Due to the unique features of image data that distinguish it from text structure data, such as high redundancy and correlation and large storage capacity, traditional encryption schemes such as Data Encryption Standard (DES) [21] and Advanced Encryption Standard (AES) [22] are not feasible for real-time applications.

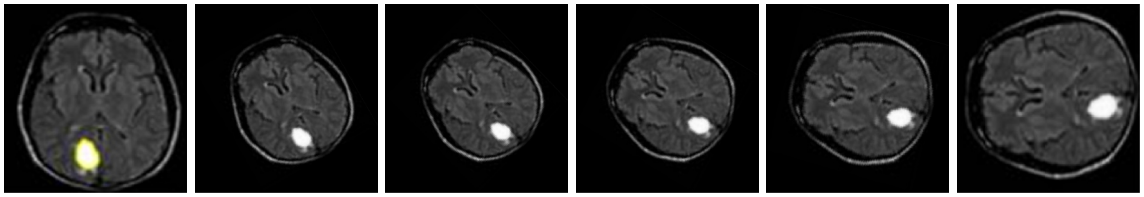

(a) Original MRI (b) Original MRI (c) Flipped at 30^0 (d) Flipped at 45^0 (e) Flipped at 60^0 (f) Flipped at 75^0

FIGURE 5 Original and corresponding flipped versions of an MRI Image.

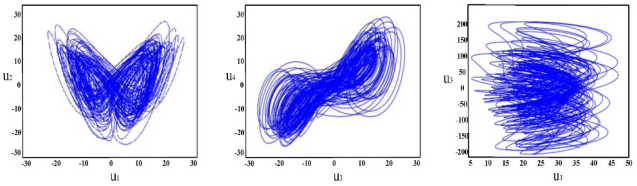

(a) $u_1 - u_2$ (b) $u_3 - u_4$ (c) $u_1 - u_3$

FIGURE 6 The hyperchaotic behaviour of SHCM.

4.1 | Hyperchaotic map

We propose to use a seven-dimensional ($7D$) Hyper chaotic map (SHCM), developed by Yang et al. [57] to secure the BMIs in our dataset. SHCM integrates a six-dimensional ($6D$) hyperchaotic [58] and one-dimensional ($1D$) linear maps. It exhibits complicated behaviour yet has a straightforward algebraic framework. SHCM contains five positive Lyapunov exponents (*LEs*), indicating that it is very complex and superior to lower-dimensional maps. Moreover, the large number of initial parameters that can be used as secret keys offers a large size key, making the encryption algorithm resistant to brute force attacks. The mathematical formulation of SHCM is given in Equation (1).

$$\begin{cases} y_1' = h(y_2 - y_1) + y_4 + dy_6, \\ y_2' = e(y_1 - y_2) - y_1 y_3 + y_5, \\ y_3' = -fy_3 + y_1 y_2, \\ y_4' = gy_4 - y_1 y_3, \\ y_5' = -Ly_2 + y_6, \\ y_6' = p_1 y_1 + p_2 y_2, \\ y_7' = ky_7 + my_4, \end{cases} \tag{1}$$

where $y_1, y_2, \ldots, y_7$ correspond to the initial conditions or secret keys of SHCM. The coupling parameter is denoted by m. The constant parameters are h, f, and e. The control parameters are d, $g, L, p1, p2$, and k. The hyperchaotic behaviour of SHCM is shown in Figure 6 using the parameters $h = 10$, m $= 1$, $L = 9.9, f = 83$, $d = 1, p_1 = 1, e = 28, g = 2, p_2 = 2$, and$k = 1$. It also has seven Lyapunov exponents (*LEs*) and a very rare unstable equilibrium $Q(0, 0, 0, 0, 0, 0, 0)$. The obtained LEs for SHCM are $LE_1 = 1$, $LE_2 = 0.4128$, $LE_3 = 0.2255$, $LE_4 = 0.1360$, $LE_5 = 0.0880$, $LE_6 = 0.0000$, *and*$LE_7 = 12.5289$. The eigen values of the corresponding LEs are $E_1 = 22.06230, E_2 = 2.6667, E_3 = 1, E_4 = 2$, $E_5 = 11.4755$, *and*$E_{6,7} = 0.0370.3850i$. As can be shown, SHCM may construct five positive *LEs* with just one equilibrium.

4.2 | Encryption algorithm

Apart from hyperchaotic maps, the proposed encryption method employs a bit-plane encryption technique that decomposes the BMI into its eight bit-planes (BPs). The purpose of extracting the BPs from the plaintext image is to create confusion or permutation in the plaintext image at the bit-level because, as stated in Ref. [59], any encryption technique is considered more secure if it encrypts the digital image at the bit-level as compared to the pixel level.

In addition to creating the permutation in the plaintext image, computing time is also a critical element. Therefore, only bit-planes containing the majority of plaintext information are considered for permutation. The percentage of information present in each bit-plane can be calculated using Equation (2) [59].

$$I_k = \frac{2^{k-1}}{\sum_{k=0}^{7} 2^{k-1}} \tag{2}$$

In Table 1, the information percentage of the plaintext image contained in each bit-plane is shown, where it can be observed that over 94% of the plaintext information is included in the first four bit-planes, which are the Most Significant Bit-Planes (MSBPs).

The permutation process applied to the BPs is as follows: Let the plaintext BMI is I_{BMI} is:

$$I = \begin{bmatrix} 150 & 26 & 210 \\ 35 & 127 & 206 \\ 42 & 169 & 166 \end{bmatrix}$$

The binary version of I_{BMI} will be as follows:

$$I_{bin} = \begin{bmatrix} 10010110 & 000110100 & 11010010 \\ 00100011 & 01111111 & 11001110 \\ 00101010 & 10101001 & 10100110 \end{bmatrix}$$

To extract the BPs from I_{bin} consider each corresponding bit from each pixel. For instance, for the $BP_{8^{th}}$, choose 8th bit from

TABLE 1 Percentage information in each position of bit-plane (BP_{k+1}) [$k = 0, 1, \ldots 7$].

Position	Information %
1	0.30
2	0.79
3	1.42
4	3.12
5	6.25
6	12.23
7	25.7
8	50.20

each pixel. Similarly for the $BP_{8^{th}}$, choose 7th bit form each pixel and so on. The extracted eight BPs form I_{bin} will be as follows:

$$BP_{8^{th}} = \begin{bmatrix} 0 & 1 & 1 \\ 1 & 0 & 0 \\ 0 & 1 & 0 \end{bmatrix}, BP_{7^{th}} = \begin{bmatrix} 1 & 0 & 1 \\ 1 & 1 & 1 \\ 1 & 0 & 0 \end{bmatrix}$$

$$BP_{6^{th}} = \begin{bmatrix} 1 & 0 & 1 \\ 1 & 0 & 0 \\ 1 & 0 & 1 \end{bmatrix}, BP_{5^{th}} = \begin{bmatrix} 0 & 1 & 0 \\ 1 & 1 & 1 \\ 0 & 0 & 0 \end{bmatrix}$$

$$BP_{4^{th}} = \begin{bmatrix} 0 & 0 & 1 \\ 1 & 0 & 1 \\ 1 & 0 & 1 \end{bmatrix}, BP_{3^{rd}} = \begin{bmatrix} 1 & 1 & 0 \\ 0 & 0 & 0 \\ 1 & 0 & 0 \end{bmatrix}$$

$$BP_{2^{nd}} = \begin{bmatrix} 0 & 1 & 0 \\ 1 & 0 & 1 \\ 1 & 1 & 0 \end{bmatrix}, BP_{1^{st}} = 5\begin{bmatrix} 0 & 0 & 0 \\ 0 & 0 & 0 \\ 0 & 0 & 0 \end{bmatrix}$$

If we change the positions of values present in the BPs, the permuted bit-planes (PBPs) will be as follows:

$$PBP_{8^{th}} = \begin{bmatrix} 1 & 1 & 0 \\ 0 & 0 & 0 \\ 1 & 0 & 1 \end{bmatrix}, PBP_{7^{th}} = \begin{bmatrix} 0 & 1 & 1 \\ 1 & 0 & 1 \\ 1 & 1 & 0 \end{bmatrix}$$

$$PBP_{6^{th}} = \begin{bmatrix} 0 & 1 & 0 \\ 1 & 1 & 1 \\ 0 & 0 & 1 \end{bmatrix}, PBP_{5^{th}} = \begin{bmatrix} 1 & 1 & 1 \\ 0 & 0 & 1 \\ 0 & 0 & 0 \end{bmatrix}$$

$$PBP_{4^{th}} = \begin{bmatrix} 0 & 1 & 0 \\ 0 & 0 & 1 \\ 1 & 1 & 1 \end{bmatrix} PBP_{3^{rd}} = \begin{bmatrix} 1 & 0 & 1 \\ 1 & 0 & 0 \\ 0 & 0 & 0 \end{bmatrix}$$

$$PBP_{2^{nd}} = \begin{bmatrix} 1 & 1 & 1 \\ 0 & 1 & 1 \\ 0 & 0 & 0 \end{bmatrix}, PBP_{1^{st}} = \begin{bmatrix} 0 & 0 & 0 \\ 0 & 0 & 0 \\ 0 & 0 & 0 \end{bmatrix}$$

Following the permutation process, the binary values that are placed at position (1,1) in each *PBP* are merged together to produce the eight binary values that are used for the first pixel value (1,1) of the permuted image. In a similar manner, in order to acquire the (1,2) pixel in the permuted image, combine the binary values that are inserted at the location (1,2) in each *PBP*. Repeat the same process to obtain all pixel values of the permuted image (P_{im}). The final permuted image corresponding to I_{BMI} will be as follows:

$$P_{im} = \begin{bmatrix} 10010110 & 11111010 & 01010110 \\ 01100100 & 00100010 & 01111010 \\ 11001000 & 01001000 & 10101000 \end{bmatrix}$$

$$P_{im} = \begin{bmatrix} 150 & 250 & 86 \\ 100 & 34 & 122 \\ 200 & 72 & 168 \end{bmatrix}$$

The matrix (P_{im}) is obtained by performing only a permutation operation on the bit plane, and the resulting matrix is clearly distinct from the original matrix I.

Following the extraction of bit-planes from the original image, it is divided into numerous blocks and rotated in various directions. Rotating each block creates diffusion through the XOR operation. Additionally, four distinct blocks are created, each one identical in size to the block extracted from the plaintext image. Equation (3) explains the mathematics behind such created blocks.

$$\begin{cases} b_1 = \lfloor x_i(j + 1000) \times 10^{10} \rfloor \bmod 4 \\ b_2 = \lfloor x_i(j + 1000 + L_i) \times 10^{10} \rfloor \bmod 12 \\ b_3 = \lfloor x_i(j + 1000 + 2 \times L_i) \times 10^{10} \rfloor \bmod 20 \\ b_4 = \lfloor x_i(j + 1000 + 3 \times L_i) \times 10^{10} \rfloor \bmod 28 \end{cases} \quad (3)$$

where x_i is a sequence generated using hyper chaotic map, $L_i = mn/16$. that is, mn is size of original image, flow is the function which discards the numerical digits after the decimal point. $i = 1, 2, \ldots, 4 \times mn/16$ and $j = 1, 2, \ldots, mn/16$.

The "XOR", "add" and starting block operations are very effective not only just for diffusing the effects of previous pixels, but also for enhancing the encryption effect on images having a large portion of the same pixel values.

After performing the "XOR", "summation" and block rotation operations, shift 8-bit right in the row direction to get another block that requires processing and continues horizontally until finish. Then, using 8-bit pairs, proceed down and 8-bit left shift to produce another block for further processing. The initial encryption procedure is repeated until it reaches the end of the $2m \times 2n$ matrix. Finally, an image is generated by translating this processed matrix of dimensions $2m \times 2n$ into a matrix of dimensions $m \times n$.

Due to the processing sequence from upper left to lower right, a change to a pixel might propagate to the pixels behind it. To increase the diffusion effect, an XOR operation is performed vertically from the bottom right to the upper left then perform permutation according to the random sequence generated using hyperchaotic map. The permutation operation is applied to the image's rows and columns. Numerous permutation rounds are

undertaken to ensure that the plaintext image has the highest amount of unpredictability possible.

After the first encryption step, a $1 - D$ array, denoted by Q, is generated. The XOR operation is applied to Q according to Equation (4) to generate the final encrypted image. The generalised block diagram of the proposed encryption algorithm is shown in Figure 7.

$$\begin{cases} b_1 = \lfloor x_i(j+1000) \times 10^{10} \rfloor \bmod 256 \\ E = \left[b(i) \times 10^3 + E(i+1)\right] \bmod 256 \\ \qquad \oplus \left[Q(i) + b(i) \times 10^2\right] \bmod 256 \oplus b(i) \end{cases} \tag{4}$$

Where $\oplus$ is the XOR operator. The generated secured images using the proposed encryption algorithm are displayed in Figure 8, where it is clear that the plaintext information is properly encrypted and no information can be visualised. Additionally, as indicated in Ref. [60], their corresponding histogram reveals that the plaintext information in the encrypted image is highly secured. A generalised pseudo-code of the proposed encryption algorithm is given in Algorithm 2.

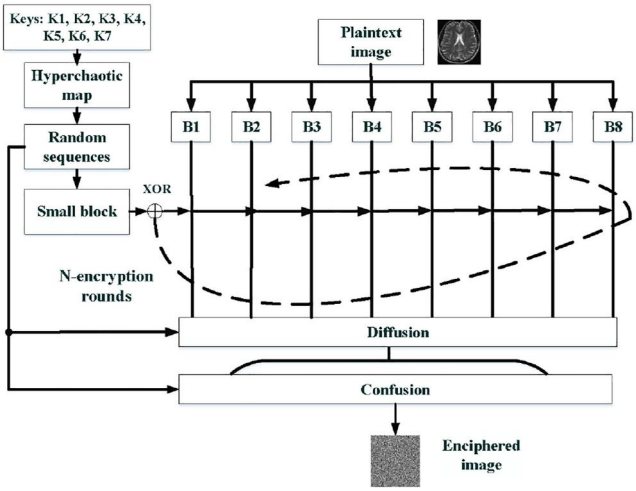

FIGURE 7 Generalised block diagram of the proposed encryption algorithm.

Algorithm 2 Pseudo code for the proposed encryption algorithm

Start
Input Original MRI images (M_{im}) of size $M \times N$
Bit-plane extraction:
for $b = 1 \rightarrow 7$ **do**
    $P_b \leftarrow \left[\frac{M_{im}}{2^b}\right] \bmod 2$
        ▷ P_1, P_2, …, P_7 are the extracted biplanes
Random sequence generation:
Iterate SHCM for one thousand times
Insert initial conditions and control parameters (K_1, K_2, …, K_7) in SHCM.
for $i = 1 \rightarrow 1000$ **do**
  Iterate Equation (1) ▷ Store results in Y_{i+1}
  $Q(i) \leftarrow Y_{i+1} \times 999$
  $F(i) \leftarrow \lfloor Q(i) \rfloor$
  $Md(i) \leftarrow F(i) \bmod 256$
$X \leftarrow$ UNIQUE($Md(i)$, 256) ▷ Choose only unique values
Change initial conditions: $\left(K'_1, K'_2, \ldots, K'_7\right)$
Repeat all the above steps to generate another random sequence (Y) for column permutation
Row permutation:
for $row = 1 \rightarrow R$ **do**
    $rowperm(X(R), :) \leftarrow M_{im}(R, :)$
Column permutation:
for $col = 1 \rightarrow N$ **do**
    $colperm(:, Y(col)) \leftarrow rowperm(:, N)$
Create diffusion using XOR operation to generate final encrypted image.
End

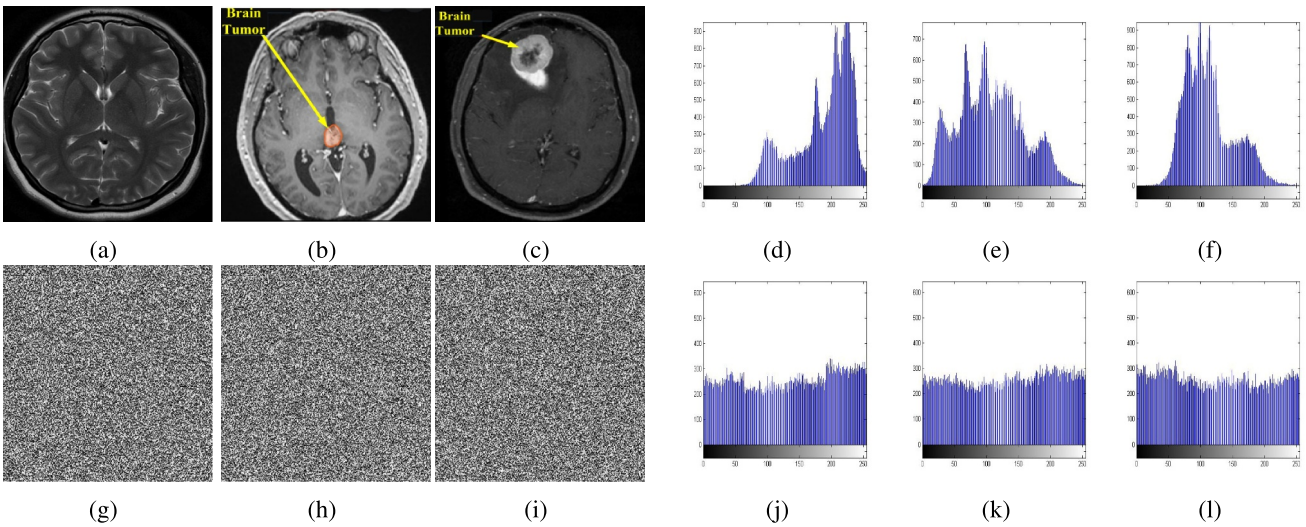

FIGURE 8 Plaintext images (a)–(c) and their histograms (d)–(e) along with their corresponding ciphertext images (g)–(i) and histograms (j)–(l).

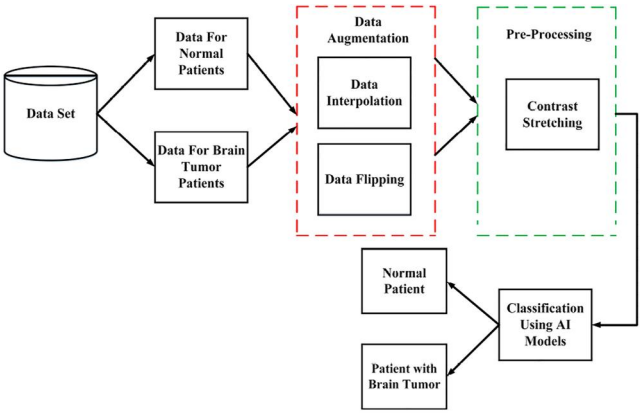

FIGURE 9 Proposed methodology for detecting brain tumour.

5 | TUMOUR DETECTION

This section provides the details of data analysis for detecting and localising tumours in BMIs. We perform several data preprocessing steps to clean noise in BMIs. The noise could be introduced due to device calibration issues or during the data augmentation phase. We also enhance the image quality for effective analysis by contrast stretching. We extract relevant image features from the preprocessed BMIs. These feature vectors are then classified using a CNN-based deep learning framework.

The overall methodology consists of three major phases: (a) data preprocessing, which includes MRI image contrast stretching and image segmentation; (b) feature extraction and (c) CNN classification as shown in Figure 9. We discuss details of each phase in the following subsections.

5.1 | Preprocessing

To enhance the image quality of the de-noised BMIs, we apply contrast stretching to them. Let I be the original BMI with $A \times B$ dimensions (A and B correspond to the number of rows and columns in BMI). The Gaussian filter (G_f) is applied to the original images for initialisation and finding the Gaussian value. A Gaussian expression can be found in Equation (5).

$$G_f = \frac{1}{\phi\sqrt{2\pi}} e^{\left(\left(I_{(a,b)}-\sigma\right)/\phi\right)^2} \tag{5}$$

where σ represents the average value of $I(a, b)$ and ϕ represents the standard deviation which is the amount of variation or randomness in the pixel values of the digital image. Once this Gaussian value is obtained, it is used in the gamma function $H(i, j)$ for contrast stretching, which enhances the contrast between the tumour area and the surrounding background pixels. The function $H(i, j)$ is described by the equations below:

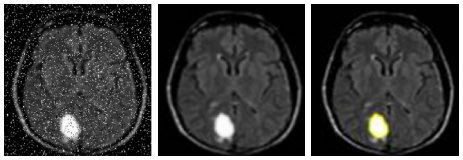

(a) Noisy BMI (b) Noise removed (c) Enhanced image

FIGURE 10 Effect of applying median and contrast filter on a sample noisy image.

$$H(i,j) = \frac{1+\sigma}{\xi} \times \Xi \tag{6}$$

$$\xi = \frac{1+G(f)}{\Upsilon} \tag{7}$$

ξ and Υ in Equations (6) and (7) represent the assisting function and the constant with a value of 0.2, respectively. The Ξ stands for a constant parameter with an initialised value of 2 [61]. The image brightness can be improved by increasing the value of Ξ. The effect of applying the median and contrast filters is displayed in Figures 10b,c, respectively.

5.2 | Feature extraction

Feature extraction is the process of gathering higher-level information such as the shape, texture, colour and contrast present in the original image. Texture analysis is a critical component of both machine learning systems and human visual perception [62].

The quality and significance of features determine the accuracy of downstream classification tasks and the subsequent medical diagnostics. A critical task in brain magnetic resonance imaging is extracting significant features due to the complex structure of diverse tissues such as white matter, grey matter and cerebrospinal fluid (CSF). A better understanding of textural observations and analysis might aid in diagnosing tumours, determining the stage of cancer and evaluating treatment responses.

Various image features have been used in different domains. Haralick et al. [63] argued that the texture features and the Gray Level Co-occurrence Matrix (GLCM) are the most frequently used features for extracting the relevant information from an image. We use a two-phase approach to extract features of BMIs. First, we compute the GLCM of images and then extract texture features based on the GLCM. The formulae for some of the relevant statistical features that we use and their brief description are given below.

Mean (μ): is calculated by summing all the pixel values in the original image, divided by the total number of pixels present in the original image, as given in Equation (8).

$$\mu = \frac{1}{A \times B} \times \sum_{i=0}^{A-1} \sum_{j=0}^{B-1} I(i,j) \tag{8}$$

Standard deviation (σ): is the value of the second moment representing a population's probability distribution and may be used to quantify inhomogeneity. A higher value of σ results in a higher degree of intensity and a greater contrast between the pixel values in the original image. The value of σ can be found using Equation (9).

$$\sigma = \sqrt{\frac{1}{A \times B} \times \sum_{i=0}^{A-1} \sum_{j=0}^{B-1} [I(i,j) - M)]^2} \tag{9}$$

Skewness ($S_k(I)$): is used to gauge symmetry, or the absence of symmetry in an image. $S_k(I)$ can be calculated using Equation (10).

$$S_k(I) = \frac{1}{A \times B} \times \frac{1}{\sigma^3} \sum [I(i,j) - M]^3 \tag{10}$$

Kurtosis ($K_k(I)$): is used to measure the probability of a random variable distribution. For the image I, its kurtosis $K_k(I)$ can be evaluated using Equation (11).

$$K_k(I) = \frac{1}{A \times B} \times \frac{1}{(\sigma)^4} \sum [I(i,j) - M]^4 \tag{11}$$

Coarseness ($Coar$): Coarseness, a measure of roughness in an image, is used to distinguish between different textures. For a constant window size, a texture with a lower number of texture elements is considered coarser than the one with a higher number. Having a rough texture corresponds to a higher coarseness value. Coarseness values are lower in fine textures than in coarse textures. It is defined as follows:

$$Coar = \frac{1}{2^{A+B}} \sum_{i=0}^{A-1} \sum_{j=0}^{B-1} I(i,j) \tag{12}$$

5.3 | CNN architecture selection

In the proposed research work, several pre-trained CNN architectures, such as MobileNetV2 [64], Densenet [65], ResNet [66], LeNET CNN [67] and EfficientNet [68] are evaluated. We select the best performing CNN architecture for the task of brain tumour detection in BMIs. As shown in Table 7, the statistical results for the several parameters are given, in which it can be seen that the LeNET gives the highest accuracy among the pretrained CNN architectures. The suggested CNN-based model, which is employed in this article, consists of two convolutional layers, two pooling layers and one fully connected neural network. The first convolutional layer has 128 convolutional filters, which are used to convolve the input BMI with the kernel of size 3 × 3 as given in Equation (13).

$$\text{Convolve output} = I(I,j) \oplus F \tag{13}$$

where $\oplus$ denote the BMIs convolution operator. F is the filter function that gives the filtered output when the original BMI and the function F are convolved with each other. In the proposed work, the function F is a linear function. Therefore, any type of padding such as zero padding, is not required.

Each convolution filter creates a large number of high-density pixels, which are incompatible with direct application to feed-forward neural networks. As a result, the sizes of filters for output data should be adjusted before feeding into the neural networks. This is accomplished via the use of layers, which are used for pooling purposes. A 2 × 2 filter mask is applied to filtered output which is generated by applying the convolution filters. The filter mask has a mean value, which is determined using the average pooling layer. Because the max-pooling layer has a high level of accuracy, it is used in the design of the proposed CNN.

Before reaching the final convolutional layer, the response of the first pooling layer is sent through the other convolutional layer, in which 256 convolutional filters are used. It is 3 × 3 in size corresponding to the kernel size of the other convolutional layer. For high classification accuracy, the number of convolutional filters in the first and second convolutional layers is calculated and fixed after multiple iterations in the first and second layers, respectively. In the response from both the layers, there is a mixture of positive and negative values to consider. It is not suitable to feed negative values directly into the pooling layer of CNN design because it results in a degradation of the functionality of the pooling units. Therefore, the convolved patterns from both layers are sent through the rectifier linear process, which changes the negative response into a positive one, and thus the result is a positive response.

By passing such filtered outputs via a second pooling layer, the second convolutional layer's output size is reduced by a factor of two. The second pooling layer performs similar functions to the first.

A fully connected feed-forward neural network (FFNN) [69] is used in the proposed work, which is designed for the categorisation of outputs from the other pooling layer. A total of two hidden layers, one input layer, and one output layer, are used in our experiments. A total of five neurons makes up the input layer, and each hidden layer has a total of twelve neurons. Two neurons are located in the output layer. The neurons in each layer are selected after a number of repetitions in order to attain the highest possible accuracy in categorisation. Specifically, the first neuron in the output layer represents the tumour case, while the second neuron is representative of non-tumour cases in the output layer.

To summarise the proposed work, a pseudo code given in Algorithm 3.

Algorithm 3 Pseudo code for classification methods

```
Start
Input: D ←Decrypted and Augmented Dataset of BMIs
Classification:
[Γ, γ] ← TestTrainSplit(D)
                    ▷ Γ is train set, γ is test set
i_Γ ←Index(Γ)    ▷ Indices of train set values
i_γ ←Index(γ)    ▷ Indices of test set values
L_{i_γ} ←Classification(D(i_Γ), L(i_Γ), D(i_γ))
▷ using CNN, SVM, RF, DT
Output: Classified Dataset of BMIs.
End
```

6 | EXPERIMENTAL SETUP AND EVALUATION MEASURES

The proposed research work is implemented using the Python open source framework and evaluated on a system having hardware specs of 8 GB RAM and a 6 GB of GPU having 6 graphics processing clusters.

6.1 | Security evaluation parameters

For the evaluation of the proposed encryption algorithm, several security parameters such as entropy, energy, contrast and correlation are considered.

Entropy (E): of an image is used to determine its degree of randomness. Higher entropy values result in less information being available in an image. Entropy may be calculated mathematically using Equation (14).

$$E(I) = \sum_{i=0}^{A-1} \sum_{j=0}^{B-1} I(i,j) \log_2 I(i,j) \tag{14}$$

Energy (E_n): is used to measure the amount of information present in the image. Higher values of energy correspond to more information. It can be calculated using Equation (15).

$$E_n(I) = \sum_{i=0}^{A-1} \sum_{j=0}^{B-1} I^2(i,j) \tag{15}$$

Contrast (*Cont*): is the measurement of the pixel intensity. Mathematically, it can be defined as follows:

$$Cont(I) = \sum_{i=0}^{A-1} \sum_{j=0}^{B-1} (i-j)^2 I(i,j) \tag{16}$$

Correlation (*Corr*): The degree of similarity between image pixels is defined by the correlation coefficient. The greater the value of correlation, the greater the similarity between the pixels. The correlation coefficients lie in the range [-1 +1]. The values −1 and +1 correspond to the negative and positive correlations, respectively. Given total pixels (K) and enciphered images in horizontal and vertical directions ($E(f)$ & $E(g)$), correlation between each pair of image pixel values (P and Q) can be calculated using the equations given below:

$$Corr(P,Q) = \frac{\frac{1}{K}\sum_{j=1}^{K}(x_i - E_n(f))(y_i - E_n(g))}{\sigma_f \sigma_g} \tag{17}$$

$$\sigma_f = \sqrt{\frac{1}{K}\sum_{j=1}^{K}(f_i - E(f))^2} \tag{18}$$

$$\sigma_g = \sqrt{\frac{1}{K}\sum_{j=1}^{K}(g_i - E(g))^2} \tag{19}$$

6.2 | Classification evaluation parameters

We have used several performance assessment parameters to gauge our proposed classification techniques. These performance matrices are calculated using the confusion matrices as shown in Table 2.

Sensitivity (S_{sen}) or Recall (R_{rcl}): of the tumour region pixels are defined by the number of tumour area pixels that are correctly identified and given by Equation (20).

$$S_{sen} = \frac{\mathrm{TP}}{\mathrm{TP} + \mathrm{FN}} \times 100 \tag{20}$$

Specificity (S_{spe}): of the tumour region pixels are defined by the number of non-effected pixels that are correctly identified and given by Equation (21).

$$S_{spe} = \frac{\mathrm{TN}}{\mathrm{TN} + \mathrm{FP}} \times 100 \tag{21}$$

Accuracy A_{acc}: of the tumour area pixels is defined by the total number of correctly detected tumour and non-tumour pixels in the final tumour area segmented brain image and given by Equation (22).

TABLE 2 Confusion matrix for calculating performance evaluating parameters for classification technique.

		Predicted	
		No	**Yes**
Actual	No	True positives (TP)	False positives (FP)
	Yes	False negatives (FN)	True negatives (TN)

$$A_{acc} = \frac{\mathrm{TP} + \mathrm{TN}}{\mathrm{TP} + \mathrm{TN} + \mathrm{FP} + \mathrm{FN}} \times 100 \quad (22)$$

Precision (P_{pre}): is defined as the number of well-identified non-tumour pixels and given by Equation (23).

$$P_{pre} = \frac{\mathrm{TP}}{\mathrm{TP} + \mathrm{FP}} \times 100 \quad (23)$$

F-Measure ($F1$): integrates accuracy and recall into a single statistic that incorporates both characteristics and given by Equation (24).

$$F1 - score = 2 \times \left[\frac{S_{sen} \times P_{pre}}{S_{sen} + P_{pre}}\right] \times 100 \quad (24)$$

7 | RESULTS AND DISCUSSION

To evaluate the performance of the proposed work, experimental results for the proposed encryption scheme and the proposed tumour detection model are conducted separately after performing data augmentation.

7.1 | Data augmentation statistics

We use an initial collection of BMIs obtained from various hospitals in Rawalpindi and Islamabad, Pakistan. A specialist doctor indicated the labelling of the brain tumour in BMIs. We augment this dataset with additional synthetically generated BMIs using our data augmentation scheme. The dataset we use for evaluation contains 5960 BMIs, of which 4424 are taken from several hospitals. The remaining 1536 BMIs are generated using our data inflation method. The detailed dataset statistics are provided in Table 3.

A tiny section of the dataset is shown in Table 4 in which data interpolation and flipping is performed. The instances with the asterisk (*) sign in Table 4 are created with the interpolation method. For example, instance number 2 represents the new data point that is generated by interpolation of instances number 1 and 3. A lot of data points are added to make the dataset bigger by interpolating the same way. Similarly, the new instances created using the flipping method are mentioned in Table 4 with a double asterisk (**) sign. Despite the fact that none of the data inflation approaches provide the original data, the new data points that are produced using such techniques are highly similar to the original data points.

7.2 | Encryption evaluation results

The proposed design is evaluated in terms of the settings of the simulated environment and the metrics used in the evaluation process.

In addition to security parameters, fast performance in image encryption is crucial for real-time applications. It can be shown from Table 5 that the suggested technique is much quicker than the algorithms given in Refs. [70–74].

Detailed explanations of security parameters are given in Refs. [30, 75]. The statistical values of the security parameters for the proposed and existing encryption systems are displayed in Table 5, demonstrating that the proposed encryption technique outperforms the existing encryption schemes in terms of security and computational cost.

7.3 | Classification results

For evaluation of our classification methods, the dataset is divided into training and testing sets. For the training dataset, a total of 3335 and 964 BMIs are chosen from hospitals and inflated dataset, respectively. Similarly, remaining portion of the dataset is chosen for the testing dataset. The dataset details for the training and testing sets are provided in Table 6.

A few pre-trained deep learning models, such as LeNET, MobileNetV2, Densenet, ResNet and EfficientNet are incorporated in the present work. The deep learning model known as LeNET is chosen since it offers the highest accuracy as shown in Table 7.

Figure 8a–8d shows the confusion matrices for the proposed work when CNN, NB, SVM and RF are incorporated. Confusion matrix of CNN in Figure 8a shows the least number of false positives 29/5960 and false negatives 48/5960. Such confusion matrices are used to calculate the performance assessment parameters such as accuracy, sensitivity, precision, specificity and F-score Table 8.

The percentage performance assessment parameters for different classifiers are shown in Table 9. It is evident from the classification statistics that CNN is the most suitable candidate for the proposed model using several performance evaluation metrics reported in Table 9.

Table 10 compares the results of the proposed simulation to those of other standard approaches in which brain tumour detection methodologies using machine learning and deep learning is proposed. We have implemented these comparable techniques in Python and evaluated using our proposed dataset. When comparing the proposed technique for brain tumour

Methodology	Total	Male	Female	Normal BMIs	Patients with brain tumour
Hospitals	4424	3252	1172	1239	3185
Augmentation	1536	879	657	783	753
Total	5960	4131	1829	2022	3938

TABLE 3 Data points taken from different hospitals and data inflation methodology.

TABLE 4 Texture and statistical features of images used in the proposed study. The images with * and ** represent the instances created using the interpolation and flipping methods, respectively.

BMIs	Mean (μ)	Std. dev. (σ)	Entropy (E)	Skewness (S_k)	Kurtosis (K_k)	Energy (E_n)	Contrast	Correlation	Coarseness
1	8.78	44.69	6.65	0.00563	$2.770 \times e^{-5}$	10.689	0.368	0.976	8.653
2*	8.68	43.59	5.99	0.00365	$2.632 \times e^{-5}$	9.998	0.237	0.895	8.776
3	7.99	42.49	6.49	0.00148	$3.991 \times e^{-5}$	10.123	0.210	0.798	9.886
4	9.98	41.60	6.84	0.00562	$2.531 \times e^{-5}$	10.869	0.287	0.753	7.998
5*	9.36	41.19	4.39	0.00112	$3.997 \times e^{-5}$	9.872	0.310	0.900	8.635
6	8.86	41.32	4.68	0.00129	$2.910 \times e^{-5}$	9.896	0.356	0.783	7.335
7	7.69	41.33	5.63	0.00198	$2.940 \times e^{-5}$	9.358	0.210	0.960	8.549
8*	8.54	41.23	4.86	0.00299	$2.929 \times e^{-5}$	9.328	0.265	0.432	8.665
9	8.34	43.54	5.67	0.00987	$2.266 \times e^{-5}$	9.946	0.324	0.761	8.346
10**	8.65	43.12	5.89	0.00312	$2.646 \times e^{-5}$	9.766	0.196	0.873	8.463
11**	8.64	43.13	5.87	0.00399	$2.467 \times e^{-5}$	9.312	0.553	0.378	8.996
12**	8.33	43.55	5.67	0.00468	$2.316 \times {}^{-5}$	9.556	0.346	0.778	8.345
13**	8.12	43.35	5.86	0.00113	$2.367 \times e^{-5}$	9.789	0.346	0.668	8.686
14**	8.34	43.32	5.64	0.00112	$2.687 \times e^{-5}$	9.862	0.319	0.336	8.760

TABLE 5 Comparison of the proposed and existing encryption schemes.

	Proposed work					
Encrypted MRI images	**Entropy**	**Correlation**	**Energy**	**Contrast**	**PSNR**	**Execution Time (sec)**
Normal BMI_1	256	0.0002	0.0153	9.2411	3.64	0.022
Normal BMI_2	260	−0.0052	0.0151	10.7831	5.34	0.022
Disease BMI_1	254	−0.0034	0.0155	10.7344	2.65	0.025
Disease BMI_2	257	0.0001	0.0153	10.7981	3.69	0.034
Average	258.5	−0.0011	0.0152	10.4987	3.83	0.025
Existing schemes	**Comparison**					
Ref [70]	7.9954	−0.0016	0.0157	9.9883	20.45	1.362
Ref [71]	7.9956	0.0004	0.0153	9.9785	14.37	1.397
Ref [72]	7.9927	−0.0074	0.0163	9.9943	17.68	2.975

detection to other traditional approaches, it is obvious from Table 10 that the suggested approach obtained high performance ratings, specifically in terms of accuracy.

The performance measurement of multiclass classification problem is evaluated using area under the receiver operating characteristic curve (AUC-ROC). The trade-off between the false positive rate (FPR) and true positive rate (TPR) at various threshold levels is examined using AUC-ROC. The higher AUC-ROC represents a good model to distinguish between the images with tumour and normal images. The AUC-ROC of the proposed model is very close to 1 (0.977) as desired.

There are 104 images in which tumour-effected pixels are present and are classified. The proposed work divides tumour patient images into 72 "moderate" cases and 32 "severe" cases. The suggested diagnostic algorithm described in this article accurately identifies 71 out of 72 mild case images and 31 out of 32 severe case images. Thus, our suggested algorithm achieves a classification accuracy of 98.6% on mild case images and accuracy of 96.8% on severe case images.

8 | CONCLUSION

We present a CNN-based approach for accurate brain tumour prediction using BMIs. The dataset utilised in the proposed work is fully protected with an encryption scheme using hyperchaotic maps and bit-plane decomposition methods to provide high security. To enhance input quality, noise is eliminated from BMIs using median and Gaussian filters. Additionally, contrast stretching is employed to enhance the BMIs in order to extract accurate features. Furthermore, CNN is

Methodology	Phases	Total	Male	Female	Normal BMIs	Patients with brain tumour
Hospitals	Training	3335	2629	706	889	2446
	Testing	1089	629	466	350	739
	Subtotal	4424	3252	1172	1239	3185
Augmentation	Training	964	563	401	655	309
	Testing	572	316	256	128	444
	Subtotal	1536	879	657	783	753
	Total	5960	4131	1829	2022	3938

TABLE 6 Test train sets for data points taken from different hospitals and data inflation methodology.

TABLE 7 Comparison of pre-trained CNN architectures.

Architectures	A_{acc}	S_{spe}	S_{sen}	P_{pre}	$F1-score$
LeNET	98.7	97.2	99.0	99.4	99.1
MobileNetV2	93.6	91.5	92.1	92.1	95.3
Densenet	92.8	91.6	93.2	91.5	91.6
ResNet	91.6	95.4	91.6	92.4	91.7
EfficientNet	91.9	94.6	94.3	92.8	94.2

TABLE 8 Confusion matrices of different classifiers with 5960 BMIs.

		Predicted	
		No	Yes
(a) CNN			
Actual	No	4876	29
	Yes	48	1007
(b) SVM			
Actual	No	3689	153
	Yes	133	1985
(c) RF			
Actual	No	3648	202
	Yes	173	1973
(d) DT			
Actual	No	3468	159
	Yes	293	2040

TABLE 9 Comparison of the proposed model when different classifiers are used. Best results are shown in bold.

Classifiers	A_{acc}	S_{spe}	S_{sen}	P_{pre}	$F1-score$
CNN	98.7	97.2	99.0	99.4	99.1
SVM	95.2	92.8	96.5	96.0	96.2
RF	93.7	90.5	95.4	94.7	95.0
DT	92.4	92.7	92.2	95.6	93.8

employed to identify whether or not the BMIs have brain tumours. To evaluate the performance of the encryption scheme entropy, energy, contrast and correlation metrics are used. The

TABLE 10 Comparison of the proposed model with the existing ones.

Classifiers	A_{acc}	S_{spe}	S_{sen}	P_{pre}	$F1-score$
Proposed	98.7	97.2	99.0	99.4	99.1
Ref [76]	96.5	94.6	97.2	94.0	95.6
Ref [77]	95.6	96.3	97.3	94.6	96.8
Ref [78]	96.8	95.6	95.6	94.7	94.3
Ref [79]	97.5	95.8	96.3	95.8	96.8
Ref [80]	96.9	96.7	94.9	96.7	95.8

classification system is evaluated using accuracy, precision, F-score, AUC-ROC and recall, and the investigation reveals that both proposed methodologies exhibit better performance than the existing ones. Our algorithm achieves a classification accuracy of 98.6% and 96.8% on mild and severe case images, respectively.

ACKNOWLEDGEMENTS

The authors are thankful to the Deanship of Scientific Research at Najran University for funding this work under the Research Groups Funding program grant code (NU/RG/SERC/12/3).

CONFLICT OF INTEREST STATEMENT

The authors declare no conflicts of interest.

DATA AVAILABILITY STATEMENT

The data used to support the findings of this study is available from the corresponding author upon request.

ORCID

Arslan Shafique https://orcid.org/0000-0001-7495-2248
Muhammad H. Zayyan https://orcid.org/0000-0001-5366-9347

REFERENCES

1. Adamson, A.S., Smith, A.: Machine learning and health care disparities in dermatology. JAMA Dermatol. 154(11), 1247–1248 (2018). https://doi.org/10.1001/jamadermatol.2018.2348
2. Shailaja, K., Seetharamulu, B., Jabbar, M.: Machine learning in healthcare: a review. In: 2018 Second International Conference on Electronics, Communication and Aerospace Technology (ICECA), pp. 910–914. IEEE (2018)

3. Rehman, M.U., et al.: Novel privacy preserving non-invasive sensing-based diagnoses of pneumonia disease leveraging deep network model. Sensors 22(2), 461 (2022). https://doi.org/10.3390/s22020461
4. Panch, T., Szolovits, P., Atun, R.: Artificial intelligence, machine learning and health systems. J. Global Health 8(2) (2018). https://doi.org/10.7189/jogh.08.020303
5. Rehman, M.U., et al.: Future forecasting of COVID-19: a supervised learning approach. Sensors 21(10), 3322 (2021). https://doi.org/10.3390/s21103322
6. Shafique, A., et al.: Noise-resistant image encryption scheme for medical images in the chaos and wavelet domain. IEEE Access 9, 59108–59130 (2021). https://doi.org/10.1109/access.2021.3071535
7. Adnan, M., et al.: Federated learning and differential privacy for medical image analysis. Sci. Rep. 12(1), 1–10 (2022). https://doi.org/10.1038/s41598-022-05539-7
8. Rehman, M.U., et al.: Infrared sensing based non-invasive initial diagnosis of chronic liver disease using ensemble learning. IEEE Sensor. J. 21(17), 19395–19406 (2021). https://doi.org/10.1109/jsen.2021.3091471
9. Bauer, S., et al.: Multiscale modeling for image analysis of brain tumor studies. IEEE Trans. Biomed. Eng. 59(1), 25–29 (2011). https://doi.org/10.1109/tbme.2011.2163406
10. Sepehrband, F., et al.: Perivascular space fluid contributes to diffusion tensor imaging changes in white matter. Neuroimage 197, 243–254 (2019). https://doi.org/10.1016/j.neuroimage.2019.04.070
11. Lee, J.K., et al.: Spaceflight-associated brain white matter microstructural changes and intracranial fluid redistribution. JAMA Neurol. 76(4), 412–419 (2019). https://doi.org/10.1001/jamaneurol.2018.4882
12. Fame, R.M., Lehtinen, M.K.: Emergence and developmental roles of the cerebrospinal fluid system. Dev. Cell 52(3), 261–275 (2020). https://doi.org/10.1016/j.devcel.2020.01.027
13. Alqazzaz, S., et al.: Automated brain tumor segmentation on multi-modal MR image using SegNet. Comput. Vis. Media 5(2), 209–219 (2019). https://doi.org/10.1007/s41095-019-0139-y
14. Mainprize, T., et al.: Blood-brain barrier opening in primary brain tumors with non-invasive MR-guided focused ultrasound: a clinical safety and feasibility study. Sci. Rep. 9(1), 1–7 (2019). https://doi.org/10.1038/s41598-018-36340-0
15. Tandel, G.S., et al.: A review on a deep learning perspective in brain cancer classification. Cancers 11(1), 111 (2019). https://doi.org/10.3390/cancers11010111
16. Viswanath, P., et al.: Non-invasive assessment of telomere maintenance mechanisms in brain tumors. Nat. Commun. 12(1), 1–18 (2021). https://doi.org/10.1038/s41467-020-20312-y
17. Jing, D., et al.: Tissue clearing of both hard and soft tissue organs with the PEGASOS method. Cell Res. 28(8), 803–818 (2018). https://doi.org/10.1038/s41422-018-0049-z
18. Smith, S.M., et al.: Brain aging comprises many modes of structural and functional change with distinct genetic and biophysical associations. Elife 9, e52677 (2020). https://doi.org/10.7554/elife.52677
19. Women, P., et al.: American Medical Association diagnostic and treatment guidelines on domestic violence. Arch. Fam. Med. 1, 39 (1992)
20. Hussain, I., et al.: A Novel Encryption Algorithm Using Multiple Semifield S-Boxes Based on Permutation of Symmetric Group (2020). arXiv preprint arXiv:2004.12264
21. Standard, D.E., et al.: Data Encryption Standard, vol. 112. Federal Information Processing Standards Publication (1999)
22. Daemen, J., Rijmen, V.: Reijndael: the advanced encryption standard. Dr. Dobb's J. Softw. Tools Prof. Program. 26(3), 137–139 (2001)
23. Rashid, M., et al.: Brain tumor detection using anisotropic filtering, SVM classifier and morphological operation from MR images. In: 2018 International Conference on Computer, Communication, Chemical, Material and Electronic Engineering (IC4ME2), pp. 1–4. IEEE (2018)
24. Maharjan, S., et al.: A novel enhanced softmax loss function for brain tumour detection using deep learning. J. Neurosci. Methods 330, 108520 (2020). https://doi.org/10.1016/j.jneumeth.2019.108520
25. Pourjabbar Kari, A., et al.: A new image encryption scheme based on hybrid chaotic maps. Multimed. Tool. Appl. 80(2), 2753–2772 (2021). https://doi.org/10.1007/s11042-020-09648-1
26. Hussain, I., Anees, A., Algarni, A.: A novel algorithm for thermal image encryption. J. Integr. Neurosci. 17(3-4), 447–461 (2018). https://doi.org/10.3233/jin-180081
27. Toktas, A., Erkan, U.: 2D fully chaotic map for image encryption constructed through a quadruple-objective optimization via artificial bee colony algorithm. Neural Comput. Appl. 34(6), 4295–4319 (2022). https://doi.org/10.1007/s00521-021-06552-z
28. Anees, A., Gondal, M.A.: Construction of nonlinear component for block cipher based on one-dimensional chaotic map. 3D Research 6(2), 1–5 (2015). https://doi.org/10.1007/s13319-015-0049-4
29. Khan, F.A., et al.: A novel image encryption based on Lorenz equation, Gingerbreadman chaotic map and S 8 permutation. J. Intell. Fuzzy Syst. 33(6), 3753–3765 (2017). https://doi.org/10.3233/jifs-17656
30. Khan, J.S., Ahmad, J.: Chaos based efficient selective image encryption. Multidimens. Syst. Signal Process. 30(2), 943–961 (2019). https://doi.org/10.1007/s11045-018-0589-x
31. Girdhar, A., Kapur, H., Kumar, V.: A novel grayscale image encryption approach based on chaotic maps and image blocks. Appl. Phys. B 127(3), 1–12 (2021). https://doi.org/10.1007/s00340-021-07585-x
32. Talhaoui, M.Z., Wang, X.: A new fractional one dimensional chaotic map and its application in high-speed image encryption. Inf. Sci. 550, 13–26 (2021). https://doi.org/10.1016/j.ins.2020.10.048
33. Ravichandran, D., et al.: An efficient medical image encryption using hybrid DNA computing and chaos in transform domain. Med. Biol. Eng. Comput. 59(3), 589–605 (2021). https://doi.org/10.1007/s11517-021-02328-8
34. Bhogal, R.S., et al.: Medical image encryption using chaotic map improved advanced encryption standard. Int. J. Inf. Technol. Comput. Sci. 10(8), 1–10 (2018). https://doi.org/10.5815/ijitcs.2018.08.01
35. Bansal, S., Kaur, S., Kaur, N.: Enhancement in brain image segmentation using swarm ant lion algorithm. Int. J. Innovative Technol. Explor. Eng. 8(10), 1–6 (2019). https://doi.org/10.35940/ijitee.j8827.0881019
36. Rajagopal, R.: Glioma brain tumor detection and segmentation using weighting random forest classifier with optimized ant colony features. Int. J. Imag. Syst. Technol. 29(3), 353–359 (2019). https://doi.org/10.1002/ima.22331
37. Deepak, S., Ameer, P.: Automated categorization of brain tumor from mri using cnn features and svm. J. Ambient Intell. Hum. Comput. 12(8), 8357–8369 (2021). https://doi.org/10.1007/s12652-020-02568-w
38. Lorenzo, P.R., et al.: Segmenting brain tumors from FLAIR MRI using fully convolutional neural networks. Comput. Methods Progr. Biomed. 176, 135–148 (2019). https://doi.org/10.1016/j.cmpb.2019.05.006
39. Hashemzehi, R., et al.: Detection of brain tumors from MRI images base on deep learning using hybrid model CNN and NADE. Biocybern. Biomed. Eng. 40(3), 1225–1232 (2020). https://doi.org/10.1016/j.bbe.2020.06.001
40. Khan, H.A., et al.: Brain tumor classification in MRI image using convolutional neural network. Math. Biosci. Eng. 17(5), 6203–6216 (2020). https://doi.org/10.3934/mbe.2020328
41. Bousselham, A., et al.: Towards reinforced brain tumor segmentation on MRI images based on temperature changes on pathologic area. Int. J. Biomed. Imag. 2019, 1–18 (2019). https://doi.org/10.1155/2019/1758948
42. Alqudah, A.M., et al.: Brain Tumor Classification Using Deep Learning Technique–A Comparison between Cropped, Uncropped, and Segmented Lesion Images with Different Sizes (2020). arXiv preprint arXiv:2001.08844
43. Sheela, C., Suganthi, G.: Morphological edge detection and brain tumor segmentation in Magnetic Resonance (MR) images based on region growing and performance evaluation of modified Fuzzy C-Means (FCM) algorithm. Multimed. Tool. Appl. 79(25), 17483–17496 (2020). https://doi.org/10.1007/s11042-020-08636-9
44. Rao, C.H., Naganjaneyulu, P., Prasad, K.S.: Brain tumor detection and segmentation using conditional random field. In: 2017 IEEE 7th International Advance Computing Conference (IACC), pp. 807–810. IEEE (2017)
45. Sasikala, M., Kumaravel, N.: A wavelet-based optimal texture feature set for classification of brain tumours. J. Med. Eng. Technol. 32(3), 198–205 (2008). https://doi.org/10.1080/03091900701455524

46. Daniel, M.C., Ruxandra, L.M.: Brain tumor classification using pretrained convolutional neural networks. In: 2021 16th International Conference on Engineering of Modern Electric Systems (EMES), pp. 1–4. IEEE (2021)
47. Khawaldeh, S., et al.: Noninvasive grading of glioma tumor using magnetic resonance imaging with convolutional neural networks. Appl. Sci. 8(1), 27 (2017). https://doi.org/10.3390/app8010027
48. Pereira, S., et al.: Brain tumor segmentation using convolutional neural networks in MRI images. IEEE Trans. Med. Imag. 35(5), 1240–1251 (2016). https://doi.org/10.1109/tmi.2016.2538465
49. Kong, Y., Deng, Y., Dai, Q.: Discriminative clustering and feature selection for brain MRI segmentation. IEEE Signal Process. Lett. 22(5), 573–577 (2014)
50. Islam, A., Reza, S.M., Iftekharuddin, K.M.: Multifractal texture estimation for detection and segmentation of brain tumors. IEEE Trans. Biomed. Eng. 60(11), 3204–3215 (2013). https://doi.org/10.1109/tbme.2013.2271383
51. Yu, Y., et al.: Clinical big data and deep learning: applications, challenges, and future outlooks. Big Data Mini. Anal. 2(4), 288–305 (2019). https://doi.org/10.26599/bdma.2019.9020007
52. Ruprecht, D., Muller, H.: Image warping with scattered data interpolation. IEEE Comput. Graph. Appl. 15(2), 37–43 (1995). https://doi.org/10.1109/38.365004
53. Thabit, F., Alhomdy, S., Jagtap, S.: A new data security algorithm for the cloud computing based on genetics techniques and logical-mathematical functions. Int. J. Intell. Network 2, 18–33 (2021). https://doi.org/10.1016/j.ijin.2021.03.001
54. Chinnasamy, P., et al.: Efficient data security using hybrid cryptography on cloud computing. In: Inventive Communication and Computational Technologies, pp. 537–547. Springer (2021)
55. Kagita, M.K., et al.: A review on security and privacy of internet of medical things. In: Intelligent Internet of Things for Healthcare and Industry, pp. 171–187. Springer (2022)
56. Hussain, I., et al.: Construction of S-box based on chaotic map and algebraic structures. Symmetry 11(3), 351 (2019). https://doi.org/10.3390/sym11030351
57. Hu, Z., Chan, C.-K.: A 7-D hyperchaotic system-based encryption scheme for secure fast-OFDM-PON. J. Lightwave Technol. 36(16), 3373–3381 (2018). https://doi.org/10.1109/jlt.2018.2841042
58. Singh, J., Roy, B.: A novel hyperchaotic system with stable and unstable line of equilibria and sigma shaped poincare map. IFAC-PapersOnLine 49(1), 526–531 (2016). https://doi.org/10.1016/j.ifacol.2016.03.108
59. Tang, Z., et al.: Multiple-image encryption with bit-plane decomposition and chaotic maps. Opt Laser. Eng. 80, 1–11 (2016). https://doi.org/10.1016/j.optlaseng.2015.12.004
60. Hussain, I., et al.: Construction of chaotic quantum magnets and matrix Lorenz systems S-boxes and their applications. Chin. J. Phys. 56(4), 1609–1621 (2018). https://doi.org/10.1016/j.cjph.2018.04.013
61. Rotaru, C., Graf, T., Zhang, J.: Color image segmentation in HSI space for automotive applications. J. R. Time Image Process. 3(4), 311–322 (2008). https://doi.org/10.1007/s11554-008-0078-9
62. Karanja, E.M., Masupe, S., Jeffrey, M.G.: Analysis of internet of things malware using image texture features and machine learning techniques. Internet Things 9, 100153 (2020). https://doi.org/10.1016/j.iot.2019.100153
63. Haralick, R.M., Shanmugam, K., Dinstein, I.H.: Textural features for image classification. IEEE Trans. Syst. Man Cybern. 6, 610–621 (1973). https://doi.org/10.1109/tsmc.1973.4309314
64. Nguyen, H.: Fast object detection framework based on mobilenetv2 architecture and enhanced feature pyramid. J. Theor. Appl. Inf. Technol. 98(05) (2020)
65. Zhang, K., et al.: Multiple feature reweight densenet for image classification. IEEE Access 7, 9872–9880 (2019). https://doi.org/10.1109/access.2018.2890127
66. Lin, H., Jegelka, S.: Resnet with one-neuron hidden layers is a universal approximator. Adv. Neural Inf. Process. Syst. 31 (2018)
67. Kayed, M., Anter, A., Mohamed, H.: Classification of garments from fashion MNIST dataset using CNN LeNet-5 architecture. In: 2020 International Conference on Innovative Trends in Communication and Computer Engineering (ITCE), pp. 238–243. IEEE (2020)
68. Marques, G., Agarwal, D., de la Torre Díez, I.: Automated medical diagnosis of COVID-19 through EfficientNet convolutional neural network. Appl. Soft Comput. 96, 106691 (2020). https://doi.org/10.1016/j.asoc.2020.106691
69. Ghaderi, A., Morovati, V., Dargazany, R.: A physics-informed assembly of feed-forward neural network engines to predict inelasticity in cross-linked polymers. Polymers 12(11), 2628 (2020). https://doi.org/10.3390/polym12112628
70. Anees, A.: An image encryption scheme based on lorenz system for low profile applications. 3D Research 6(3), 1–10 (2015). https://doi.org/10.1007/s13319-015-0059-2
71. Wang, X., Liu, C., Jiang, D.: A novel triple-image encryption and hiding algorithm based on chaos, compressive sensing and 3D DCT. Inf. Sci. 574, 505–527 (2021). https://doi.org/10.1016/j.ins.2021.06.032
72. Farah, M.B., et al.: A novel chaos based optical image encryption using fractional Fourier transform and DNA sequence operation. Opt Laser. Technol. 121, 105777 (2020). https://doi.org/10.1016/j.optlastec.2019.105777
73. Arab, A., Rostami, M.J., Ghavami, B.: An image encryption method based on chaos system and AES algorithm. J. Supercomput. 75(10), 6663–6682 (2019). https://doi.org/10.1007/s11227-019-02878-7
74. Zhang, Y.: The fast image encryption algorithm based on lifting scheme and chaos. Inf. Sci. 520, 177–194 (2020). https://doi.org/10.1016/j.ins.2020.02.012
75. Ahmad, J., Ahmed, F.: Efficiency analysis and security evaluation of image encryption schemes. Computing 23, 25 (2010)
76. Saba, T., et al.: Brain tumor detection using fusion of hand crafted and deep learning features. Cognit. Syst. Res. 59, 221–230 (2020). https://doi.org/10.1016/j.cogsys.2019.09.007
77. Kumar, S., et al.: Automated brain tumour detection using deep learning via convolution neural networks (CNN). Int. J. Cur. Res. Rev 13(02), 148–153 (2021). https://doi.org/10.31782/ijcrr.2021.13234
78. Jian, A., et al.: Foundations of multiparametric brain tumour imaging characterisation using machine learning. In: Machine Learning in Clinical Neuroscience, pp. 183–193. Springer (2022)
79. Sekhar, A., et al.: Brain tumor classification using fine-tuned GoogLeNet features and machine learning algorithms: IoMT enabled CAD system. IEEE J. Biomed. Health Inf. 26(3), 983–991 (2021). https://doi.org/10.1109/jbhi.2021.3100758
80. Razzak, M.I., Imran, M., Xu, G.: Efficient brain tumor segmentation with multiscale two-pathway-group conventional neural networks. IEEE J. Biomed. Health Inf. 23(5), 1911–1919 (2018). https://doi.org/10.1109/jbhi.2018.2874033

How to cite this article: Rehman, M.U., et al.: An efficient deep learning model for brain tumour detection with privacy preservation. CAAI Trans. Intell. Technol. 1–16 (2023). https://doi.org/10.1049/cit2.12254